JOURNAL OF AIRCRAFT
Vol. 33, No. 1, January–February 1996

Aerodynamic Interaction Study of the Propeller/Wing Under Different Flow Configurations

J. Y. Chiaramonte,* D. Favier,† C. Maresca,† and S. Benneceur‡
Institut de Recherche sur les Phénomènes Hors Equilibre, 13009 Marseille, France

Interactional aerodynamics could significantly affect the rotary wing performance, the airframe loads, as well as the handling qualities of aircraft. It has become necessary for the nature of the vortical slipstream and its interference with aircraft components to be understood over a wide range of flight operating conditions. The propeller/wing aerodynamic interaction phenomena have been experimentally investigated at low subsonic speeds on a propeller/nacelle/half-wing configuration (P/N/W2). The P/N/W2 ensemble has been studied under different wind-tunnel flow configurations to simulate different conditions of the whole flight envelope including axial, conversion/reconversion, and hovering flights. The experimental investigation has been based on extensive overall and local data measurements performed on the propeller, the wake geometry, and the half-wing. The results exhibited the considerable influence of the flow configuration and the tilt angle parameter on the nature of the wake distortion due to the half-wing. It is also shown that such tip vortex trajectories distortions strongly affect both the instantaneous and mean lift and drag distributions along the half-wing span.

Nomenclature

C_D = drag coefficient of the half-wing, $Dr/0.5\rho V_\infty^2 S$
C_L = lift coefficient of the wing, $Li/0.5\rho V_\infty^2 S$
C_M = moment coefficient of the half-wing, $M/0.5\rho V_\infty^2 Sc$
Cp = pressure coefficient, $(p - p_\infty)/0.5\rho V_\infty^2$
Cp' = pressure coefficient in hover, $(p - p_\infty)/\rho n^2 D^2$
c = wing chord section, 1.02 m
Dr, Li = drag and lift airloads of the half-wing, N
d = distance between the propeller disk and the leading edge of the wing, $0.6R$
$L1$ = half-wing span, 0.75 m
$L2$, $L3$, $L4$ = lengths defined in Fig. 3, $L2 = 0.25$ m, $L3 = 0.10$ m, $L4 = 0.20$ m
M = pitching moment of the half-wing, mN
n = propeller rotational frequency, rps
$OXYZ$ = coordinates system defined in Fig. 1
P, T = power and thrust of the propeller
p, p_t, p_∞ = static pressure, total pressure, and pressure at infinity, Pa
R = propeller radius, 0.425 m
r = radial coordinate from the axis of rotation, m
r_t = radial coordinate of tip vortex, m
t = time, s
U, V, W = velocity components defined in Fig. 1, m/s
V_∞ = velocity at infinity, m/s
X = spanwise coordinate of the nacelle/wing ensemble, m
Z_t = axial coordinate of tip vortex, m
α = geometric incidence of the propeller/nacelle/wing configuration, deg
α_0 = mean pitch angle at $r/R = 0.70$ of the propeller blade, deg
α_1 = wing geometric incidence at zero lift line, -2 deg
β = tilt angle of propeller/nacelle around the half-wing, deg
γ = propeller operating parameter, V_∞/nD
η = propeller efficiency, $\gamma\tau/\chi$
ν = kinematic viscosity, m^2/s
ρ = air density, kg/m^3
τ = propeller thrust coefficient, $T/\rho n^2 D^4$
ϕ_i = i.d. circle of the octagonal test section, 3 m
χ = propeller power coefficient, $P/\rho n^3 D^5$
ψ, ψ_t = age of the vortex, deg
ψ_b = blade azimuth angle, Ωt deg
Ω = propeller rotational frequency, rad/s
ωt = phase of the period, deg

Subscripts
i, ind = relative to induced quantities
∞ = relative to uniform flow conditions

Superscript
$\bar{\ }$ = time-averaged quantities over a rotational period

Introduction

THE tilt-rotor aircraft configuration ideally combined the aerodynamic qualities and the advantages of both helicopter rotors and aircraft performances. However, interference effects between the rotary wing and the aircraft components can strongly affect the aerodynamic performance as well as the aircraft stability control and noise generation. As pointed out in several earlier studies,[1–7] better knowledge of such complex interference effects has become necessary. As an example, the design problem becomes particularly critical in such research programs as the Eurofar Tilt-Rotor project.[1,2] Interactional aerodynamic phenomena have been mainly studied on propeller/wing configurations[3–5] with zero value

---

Presented as Paper 94-1921 at the AIAA 12th Applied Aerodynamics Conference, Colorado Springs, CO, June 20–23, 1994; received Aug. 2, 1994; revision received April 27, 1995; revision received June 24, 1995. Copyright © 1994 by the American Institute of Aeronautics and Astronautics, Inc. All rights reserved.

*Research Engineer, UM-138 du C.N.R.S., Universités d'Aix-Marseille I & II Laboratoire ASI/IRPHE, 163 avenue de Luminy. Member AIAA.

†Senior Research Scientist, UM-138 du C.N.R.S., Universités d'Aix-Marseille I & II Laboratoire ASI/IRPHE, 163 avenue de Luminy. Member AIAA.

‡Graduate Student, UM-138 du C.N.R.S., Universités d'Aix-Marseille I & II Laboratoire ASI/IRPHE, 163 avenue de Luminy.

for β (axial flight). In such a flight configuration the wing mean performance response over the rotational period has been determined for different propeller advance ratio parameters of the propeller. Specifically, the influences of the propeller-induced upwash and downwash regions on the spanwise mean lift and mean drag wing distributions have been identified.

Some other works have been conducted on simplified rotor/body configurations[6,7] and interactional effects have been studied by means of both theoretical and experimental approaches. Instantaneous aspects of the physics of interaction has then been investigated[6] by means of unsteady pressure loads recorded at different points of the body of revolution representing a helicopter fuselage. Also, a shadowgraph visualization technique has been used to obtain quantitative information on the tip vortex trajectories[7] and on the corresponding wake distortion of the hovering rotor, with and without the body. Such kinds of unsteady data provided a more comprehensive picture of the interactional effects and are of valuable guidance in the development of numerical tools for modeling the interaction problem. However, except for the hovering flight and to some extent the axial flight configurations, the lack of experimental data available in some other important configurations (especially for conversion or reconversion flight with a tilt angle varying in the range $0 < \beta < 90$ deg), render the interactional problem difficult to model properly.

In the present study, an experimental approach was adopted to get better insight into the unsteady aerodynamic mechanisms that characterize the convertible configuration operating at different values of β (varying from 0 to 90 deg). To this end, the tested model consists of a propeller/nacelle/half-wing (P/N/W2), which is operating in different subsonic flow configurations selected to simulate the different convertible flight phases. Several works from the present group have been previously done to investigate the aerodynamics of either the isolated propeller case[8,9] or the interference effects generated on a propeller/nacelle/complete wing (P/N/W) configuration[10-12] (with $\beta = 0$ deg). These previous data will serve as a reference database to the present results.

The primary objective of this work was to investigate the interactional effects generated on the P/N/W2 configurations for different values of β. This includes the determination of the instantaneous wake geometry distortion associated to different β values, the influence of the distorted propeller slipstream on the loads distribution along the half-wing span, and the reciprocal influence of the half-wing on the overall propeller performance. The wind-tunnel investigation was conducted by means of a series of overall forces and moments measurements, unsteady local chordwise pressure distributions performed at different spanwise sections of the half-wing, and wake flow measurements characterizing the vortex distortions and instantaneous aspects of the interaction problem.

Experimental Facilities and Measurement Techniques

The tests were performed at the ASI Laboratory on a scale model of a P/N/W2 mounted in the V1 test section of S1-Luminy subsonic wind tunnel (octagonal test section, i.d. = 3 m; length of the test section, 6 m; and freestream velocity, 5 m/s $\le V_\infty \le$ 100 m/s). As shown in Fig. 1, the setup includes the model propeller, the nacelle, and the half-wing. Four flow configurations were investigated, as shown in Fig. 2: hovering flight ($\beta = 90$ deg), conversion or reconversion flight ($\beta = 60$ and 30 deg), and axial flight ($\beta = 0$ deg). The propeller was a four-bladed model of radius $R = 0.425$ m. The blade uses the NACA 64A408 airfoil series. The tips are rectangular and the twist law is a nonlinear function of the blade radius as documented in Refs. 10 and 11.

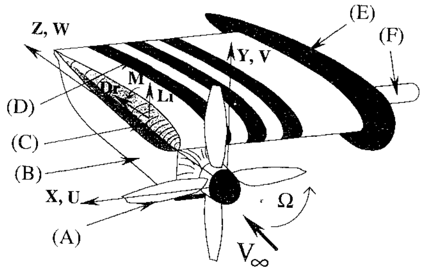

Fig. 1 P/N/W2 configuration: (A) propeller, (B) nacelle, (C) salmon shape, (D) half-wing, (E) end plate, and (F) mast.

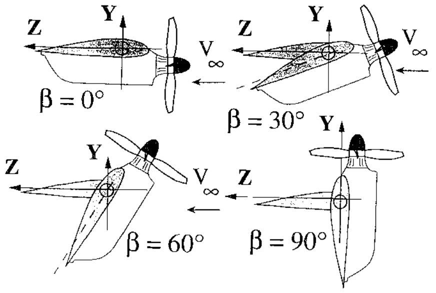

Fig. 2 Different flight phases of convertible P/N/W2 configuration.

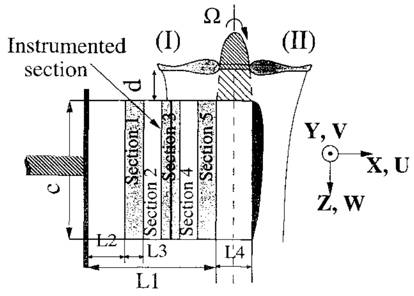

Fig. 3 Top view of the P/N/W2 setup ($\beta = 0$ deg): (I) up-going blade and (II) down-going blade.

The half-wing had a constant RA18-43N1L1 airfoil section of 18% maximum thickness, with $L_1 = 0.75$ m in span and $c = 1.02$ m in chord. An end plate was also mounted on only one side of the half-wing to avoid additional three-dimensional tip effects on the wing. The nacelle includes the electric motor driving the propeller. On the half-wing/nacelle ensemble a streamlined salmon shape is added at the wingtip. The model P/N/W2 is supported by a cylindrical mast perpendicular to the freestream direction (Fig. 1).

The present experimental approach uses a variety of unsteady measurement techniques suited for surveying the three-dimensional flow in the wake of the propeller and around the half-wing. More details on the measurement procedures and data reduction methods are given in Refs. 8–12 and include X hot-wire anemometry, two-dimensional laser velocimetry, flow visualization, pressure transducers, skin friction gauges, and strain gauges to characterize both the overall and local behavior of the propeller, the half-wing, and the wake propeller distortion generated by the presence of the body.

The half-wing was built by stacking different elements, as illustrated in Fig. 3. One of these elements was equipped with 20 unsteady pressure transducers and another one was equipped with 20 skin friction gauges. Local chordwise and skin friction distributions can be obtained at different positions along the wing span by moving the instrumented section of the wing. Five spanwise sections were considered: sections numbered 1, 2, 3, 4, and 5 located behind the up-going blade side, and corresponding to the spanwise locations: $X/R = -0.353$, -0.588, -0.824, -1.056, and -1.294.

Results and Discussion

Instantaneous Aspects of Interaction

The interference effects between the half-wing and the tilted propeller are shown to be significant when considering the instantaneous aspect of the interaction phenomena as a function of ψ_b. The operating conditions are the following: $\alpha_0 = 32.5$ deg, $\gamma = 0.89$, $V_\infty = 17.2$ m/s, $n = 22.7$ rps, and $\alpha = 0$ deg.

Figures 4a and 4b give some examples of the instantaneous $Cp = Cp(\psi)$ recorded on the upper and lower sides of the half-wing at spanwise section 3 and for two values of the tilt angle $\beta = 0$ and 30 deg. In the leading-edge region of the half-wing (e.g., transducers Nos. 1–6 and 17–20), the Cp waveforms recorded over a complete azimuthal revolution ($0 \le \psi \le 360$ deg) clearly exhibit the blade passage influence on the instantaneous pressure response. From the leading edge towards the trailing edge the amplitudes of pressure fluctuations due to the blade passage are shown to be attenuated and the imprint of the tip vortex path (indicated by the dotted line in Fig. 4a) passing close to the wing surface is clearly detected on the Cp waveforms.

The result of such tip vortex path deviations close to the wing surface is a strong distortion of the corresponding wake geometry. This wake geometry distortion has been determined as a function of ψ_b and the tip vortex path associated to each of the four blades has been measured using a hot-wire technique. Figures 5 and 6 give the wake geometry distortion obtained on the P/N/W2 configuration ($\beta = 0$ and 30 deg), which is also compared to the wake geometry relative to either the P/N/W configuration or to the isolated propeller case.

For the axial flight case ($\beta = 0$ deg), Fig. 5 illustrates the two azimuthal blade positions $\psi_b = 0$ and 180 deg. These plots give the coordinates $r/R = r/R(\psi_t)$ and $Z/R = Z/R(\psi_t)$ as a function of ψ_t for the vortex path generated by the blade tip (for each ψ_b). The comparison of the three curves shows that the wake geometry of the P/N/W2 configuration is significantly more distorted than the isolated propeller case, but it is also less distorted than the P/N/W configuration, with regard to the radial contraction r/R of the tip vortex. On the other hand, the convection velocities of the tip vortex (coordinate Z_t/R) of the P/N/W2 configuration are shown to be increased when compared to the two other configurations (isolated propeller and P/N/W configuration).

Concerning the tip vortex path obtained in the conversion or reconversion flight case $\beta = 30$ deg, Fig. 6 gives $\psi_b = 0$ and 180 deg. The results show that a large part of the propeller slipstream is deviated along the half-wing upper side. For $\beta = 30$ deg, the coordinates r/R are also shown to be strongly distorted. While the coordinates Z/R of the tip vortex path indicate an evolution quite similar to that of the two other configurations.

To illustrate this distortion effect, the plots in Fig. 7 give an example of the radial velocity field that is deduced from $U(\psi)$ and $V(\psi)$ velocity components measured at a fixed plane downstream from the propeller ($Z/R = 1.819$). Two radial flowfields are given in Fig. 7 and correspond to two values of $\psi_b = 0$ deg (Fig. 7a) and $\psi_b = 45$ deg (Fig. 7b). In both cases the radial flowfield mappings show the imprints of the tip

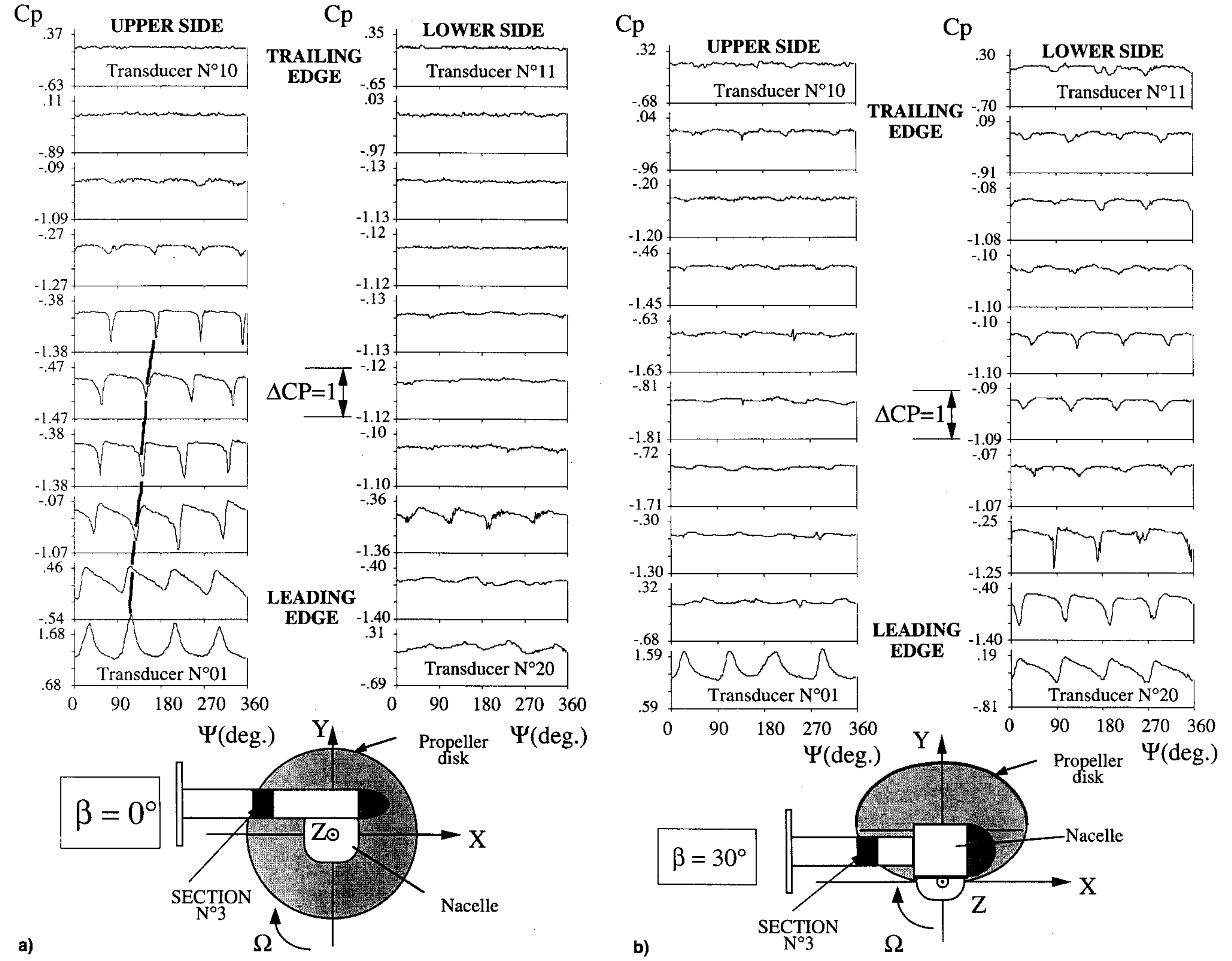

Fig. 4 Instantaneous pressure distributions on the half-wing (section no. 3). β = a) 0 and b) 30 deg.

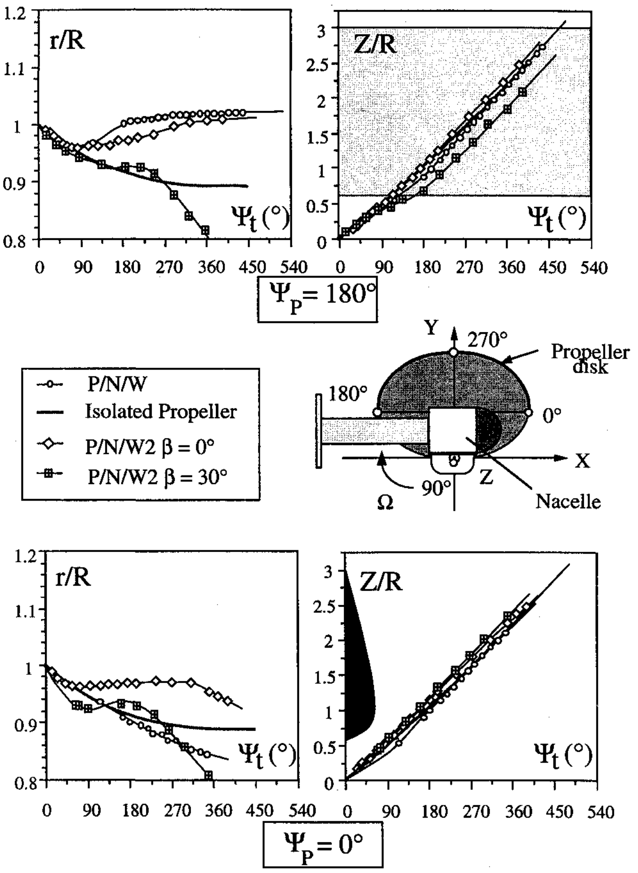

Fig. 5 Distorted tip vortex path in P/N/W2 configuration.

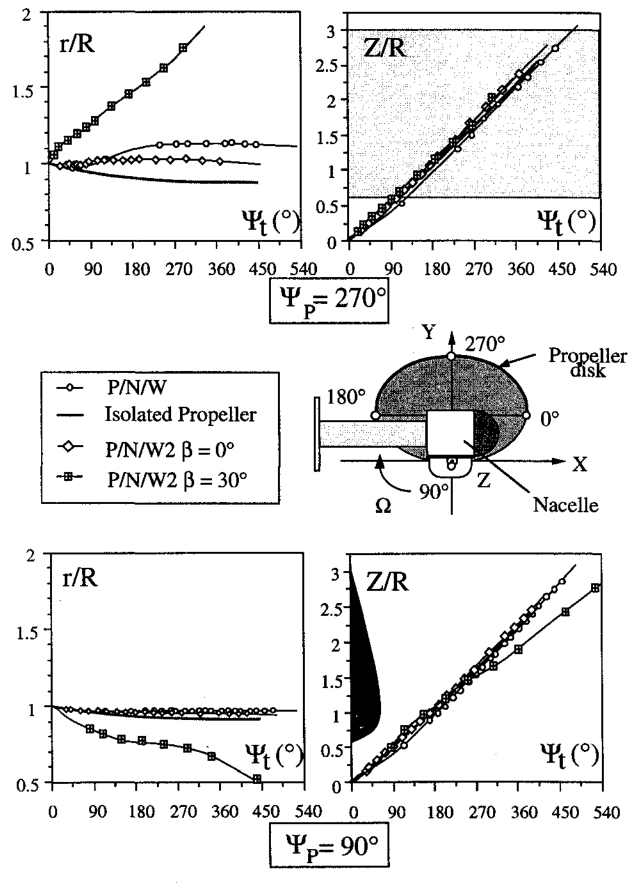

Fig. 6 Distorted tip vortex path in P/N/W2 configuration.

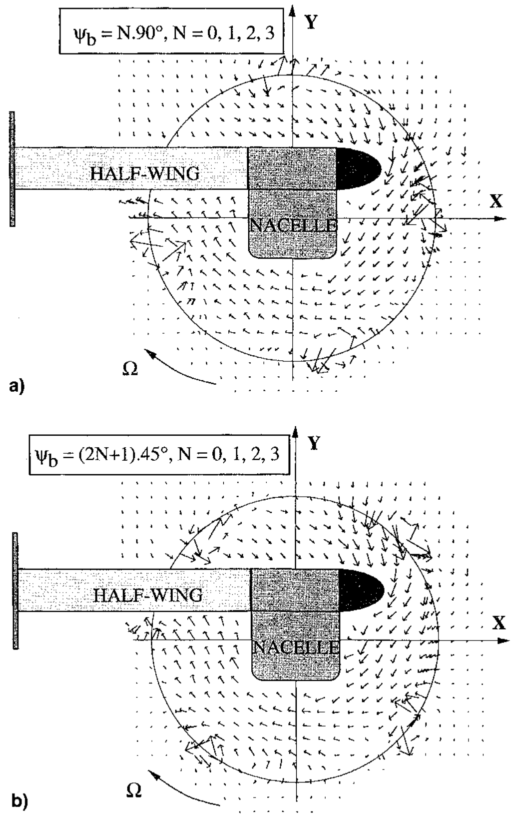

Fig. 7 Radial flowfield (Z/R = 1.819) in P/N/W2 configuration, β = 0 deg.

vortex positions. These results indicate a smooth slipstream deflection towards the $X < 0$ (e.g., in the sense of the blade rotation) on the lower side of the wing. On the upper side of the half-wing the slipstream deflection is directed towards $Y > 0$ ($Y_t/R > 1$). On the other hand, such radial velocity fields indicate a smooth wake contraction ($r_t/R < 1$) under the body of the nacelle.

Spanwise Mean Pressure and Mean Lift Distributions on the Half-Wing Surface

The pressure distributions along the upper side and lower side of the half-wing have been measured at different sections of the half-wing span numbered from 1 to 5 in Fig. 3. Results in Figs. 8 and 9 give the mean distributions $\overline{Cp}$ obtained in the steady flow configuration (without propeller) and in the unsteady flow configuration (obtained by time averaging the instantaneous values over the rotational period) at sections 1, 3, and 5 (corresponding to the blade span sections: $X/R = -1.294$, -0.823, and -0.353) and for $\beta = 0$, 30, and 60 deg. In this case the operating conditions are the following: $\alpha_0 = 32.5$ deg, $\gamma = 0.89$, $V_\infty = 17.2$ m/s, $n = 22.7$ rps, and $\alpha = 0$ deg.

At $\beta = 0$ deg in Figs. 8a and 8b, the $\overline{Cp}$ distributions obtained for the steady configuration are shown to be very similar all along the half-wing span at sections 1, 3, and 5, indicating that no crossflow effects are present on the wing. For $\beta > 0$ deg the influence of the slipstream is clearly exhibited by the corresponding $\overline{Cp}$ plots in Fig. 8c. These $\overline{Cp}$ distributions confirm the increase in the local lift coefficient when the radial position of the wing section is moved along the span from 1 to 5. Moreover, the gain in lift is also shown to be higher when β is increased at $\beta = 60$ deg (sections 3 and 5).

In the unsteady flow regime the $\overline{Cp}$ mean pressures distributions are given in Fig. 9 at sections 1, 3, and 5. Because of the influence of the propeller slipstream, the $\overline{Cp}$ distributions

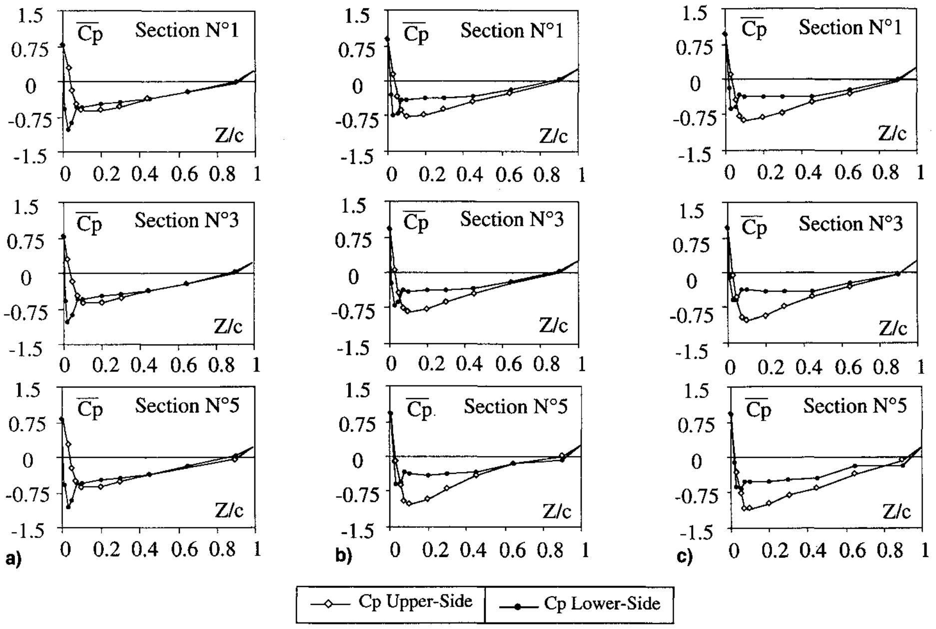

Fig. 8 Pressure distributions on the half-wing in steady flow. β = a) 0, b) 30, and c) 60 deg.

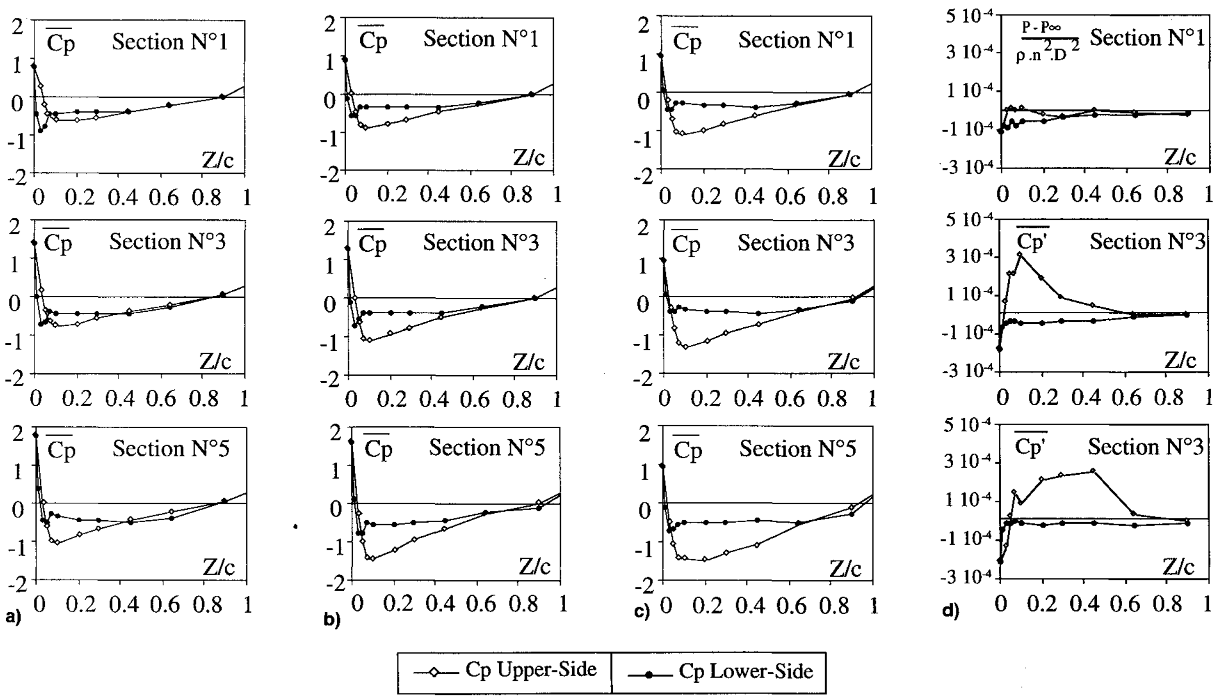

Fig. 9 Unsteady mean pressure distributions on the half-wing. β = a) 0, b) 30, c) 60, and d) 90 deg.

appear to be significantly different from the steady flow case modified for each section Z/c = constant of the wing span and at each value of $\beta = 0$, 30, and 60 deg into consideration in Figs. 9a–9c. At each value of β = constant, the results clearly indicate the presence of a low-pressure peak on the upper side of the half-wing that involves an increase of the positive local lift area near the leading edge.

At $\beta = 90$ deg, the flow hovering configuration corresponds to no upstream velocity ($V_\infty = 0$) and the pressure coefficients have thus been defined as $\overline{Cp'} = (p - p_\infty)/\rho n^2 D^2$. These $\overline{Cp'}$ are plotted in Fig. 9d and clearly exhibit the decrease in lift coefficient that occurs along the span of the half-wing from sections 1 to 5 (e.g., when moving along the span from the external region of the slipstream to the internal region of the wake flow generated by the nacelle).

This spanwise effect along the half-wing is also well confirmed when considering $\overline{C_L}$ deduced by integrating the $\overline{Cp}$ distributions along the chordwise direction Z/c, as shown to Fig. 10 for both the steady flow and the mean unsteady flow configurations. In both cases the $\overline{C_L}$ coefficient is shown to increase as β increases at all five spanwise sections investigated. However, owing to the propeller swirl influence, the unsteady flow case promotes an increase in the mean lift coefficient significantly higher than the steady flow case.

Overall Aerodynamic Coefficients on Half-Wing and Propeller

The overall half-wing aerodynamic behavior and coefficients τ and χ are given in Figs. 11–14. The plots show the evolution of the three aerodynamic coefficients C_L, C_T, and C_M measured on the complete P/N/W2 configuration as a

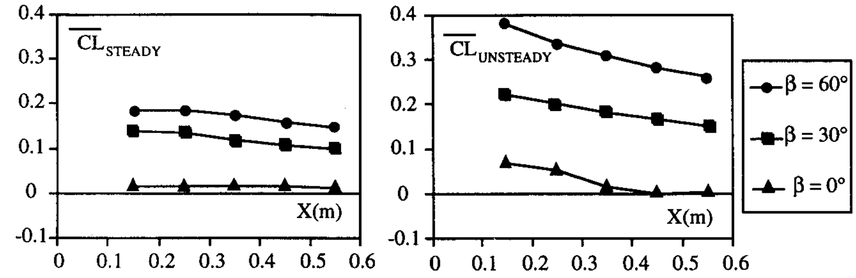

Fig. 10 Coefficient $\overline{C_L}$ of the half-wing in steady flow and unsteady flow.

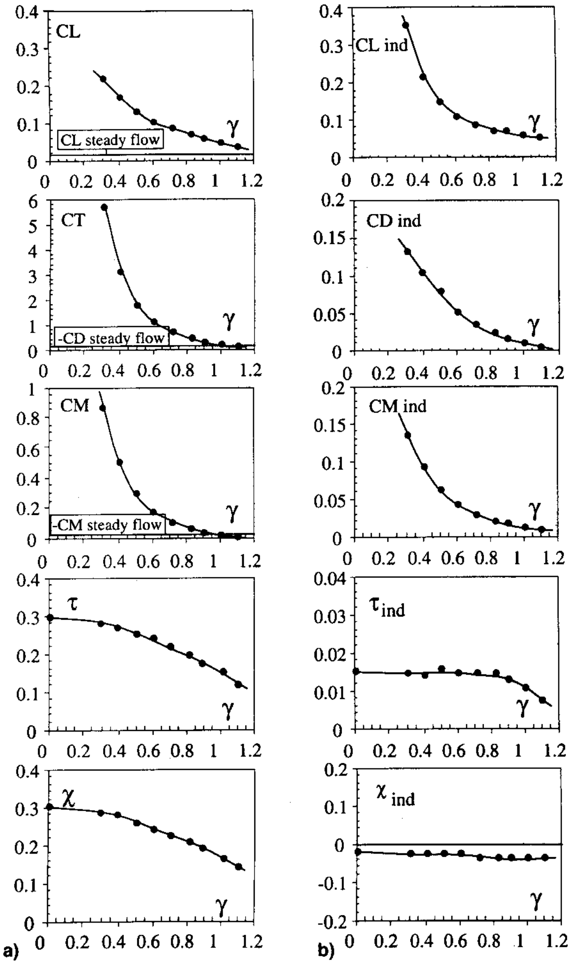

Fig. 11 Overall aerodynamic coefficients on half-wing and propeller, $\beta = 0$ deg.

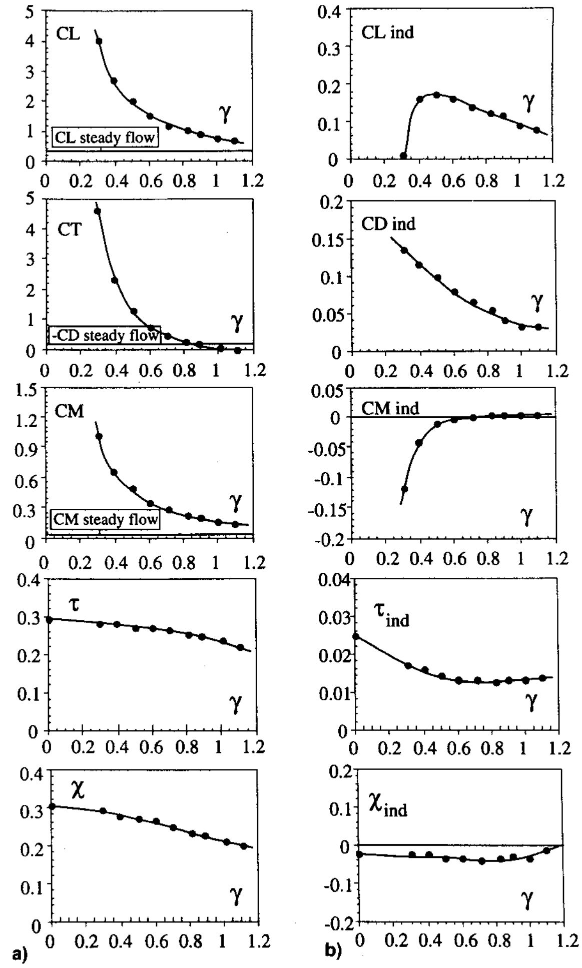

Fig. 12 Overall aerodynamic coefficients on half-wing and propeller, $\beta = 30$ deg.

function of the advancing parameter γ of the propeller ($0.3 \leq \gamma \leq 1.1$, $\alpha_0 = 32.5$ deg, $\alpha = 0$ deg). The coefficient C_T indicates a thrust coefficient when the propeller is present and loaded. These overall measurements are performed in the case of the wing placed in uniform flow and also in the case of the wing submitted to both the uniform flow and the propeller slipstream.

As β increases, the corresponding coefficient C_L is shown to increase. At $\beta > 0$ deg, this increase in the lift coefficient is due to the added components of thrust [e.g., $C_L(\beta = 30$ deg$)/C_L(\beta = 0$ deg$) = 14$, $C_L(\beta = 60$ deg$)/C_L(\beta = 30$ deg$) = 1.6$ at $\gamma = 0.6$], as shown in Figs. 11a, 12a, and 13a. The evolution of $C_T = C_T(\gamma)$ is very similar to that of $C_L = C_L(\gamma)$, and the C_T is shown to decrease when β increases from 0 to 60 deg. The increase of γ also attenuates the nose-up effect on the moment ($C_M \approx 0$ at $\gamma = 1$), however, C_M is shown to increase with β. Concerning the propeller performance coefficients, τ is also decreasing when γ or β increases. On the other hand, the increase of β involves an increase of χ for higher values of γ as shown in Figs. 11a, 12a, and 13a.

It can be mentioned that the net aerodynamic effect just described and induced by the propeller slipstream on the half-wing cannot be obtained from a direct measurement on the P/N/W2 ensemble. A series of measurements has to be performed in successive combinations of the three elements: 1) propeller, 2) nacelle, and 3) the half-wing. To this end, the experimental setup was designed in order to uncouple the half-wing from the propeller/nacelle (P/N) ensemble. In this case, the half-wing is supported by a mast system and is uncoupled to the nacelle, so that only the nacelle and propeller contributions are loaded. From such successive measurements, different algebraic operations are performed to separate the basic contribution of each element of the P/N/W2 ensemble.[10–12]

The net influence of the propeller slipstream on the wing loads has thus been obtained and is given in Figs. 11b, 12b,

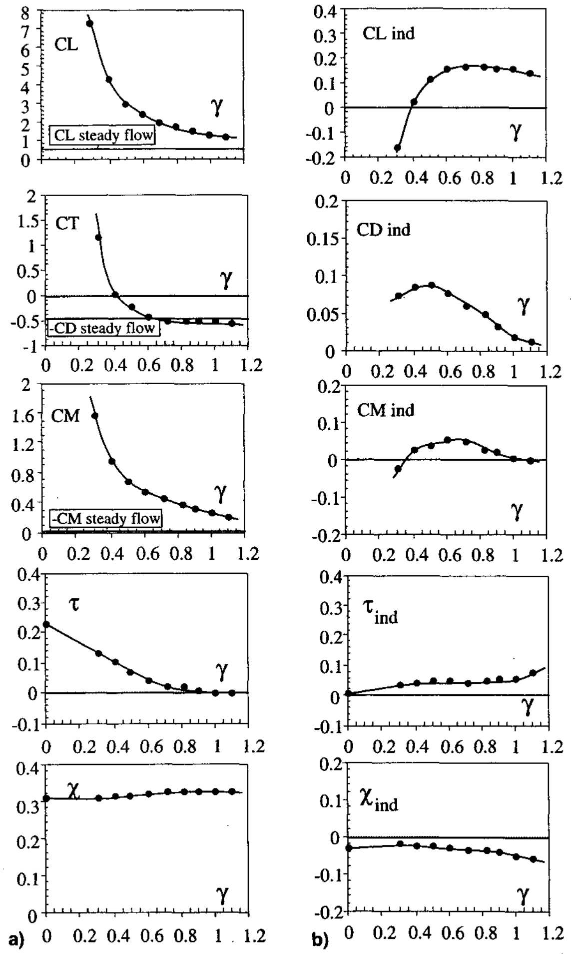

Fig. 13 Overall aerodynamic coefficients on half-wing and propeller, β = 60 deg.

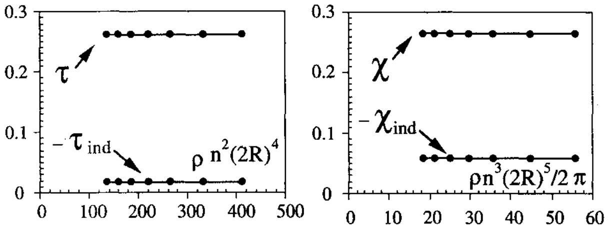

Fig. 14 Propeller performance coefficients, β = 90 deg.

and 13b. The wing aerodynamic coefficients C_{Li}, C_{Di}, and C_{Mi} correspond to the load effect of the propeller slipstream alone and are plotted as a function of γ for different values of β.

For β = 0 deg, the results in Fig. 11b indicate that the propeller swirl effect produces an important increase of the induced lift on the half-wing. The C_L obtained in steady flow is shown to be significantly lower than the $C_{L\,\text{ind}}$ induced by the propeller slipstream. However, the effect of the propeller slipstream is also to produce in the same way a strong increase on the $C_{D\text{ind}}$ of the half-wing as shown in Fig. 11b. It can be noticed that measurements of wing drag for tractor configurations obtained by Witkowski et al.[3,4] also show an induced drag increase for propeller power coefficients similar to those of the present tests, although the geometrical configuration of the test rigs was different in both experiments (especially the distance between the propeller and the fixed wing and the geometry of the nacelle).

Concerning C_{Mi}, a nose-up effect on the half-wing due to the propeller slipstream influence can also be observed. The τ_{ind} and χ_{ind} coefficients of the propeller show an evolution almost constant as a function of γ ($\tau_{\text{ind}} \approx 0.015$; $\chi_{\text{ind}} \approx -0.02$), which is due to the presence of the half-wing in the propeller slipstream.

When increasing the value β of the propeller at β = 30 deg (Fig. 12b) and β = 60 deg (Fig. 13b), the influence of the propeller slipstream is more accentuated and involves a decrease in $C_{L\,\text{ind}}$. For low γ, negative values of $C_{L\,\text{ind}}$ are reached for β = 60 deg (Fig. 13b). On the other hand, the effect on $C_{D\text{ind}}$ is shown to be more attenuated. Similar levels of $C_{D\,\text{ind}}$ are obtained at high values of γ at each of the three configurations β = constant into consideration. As β increases, a nose-down effect on $C_{M\text{ind}}$ is also observed for β = 30 deg. Concerning the influence of the half-wing presence on the propeller-induced performance (τ_{ind}, χ_{ind}), the effect is to increase the τ_{ind} coefficient as the parameter β increases. While the evolution of $\chi_{\text{ind}} = \chi_{\text{ind}}(\gamma)$ remains quite constant for the three configurations, β = constant.

A similar behavior is also obtained in the hovering configuration corresponding to β = 90 deg in Fig. 14, which is realized with the following operating parameters for the propeller: V_∞ = 0 m/s and n varying in the range: $14 \leq n \leq 25$ rps. The effect induced by the half-wing is shown to be almost constant as a function of n. In this case, the net effect due to the wing presence can be quantified by $|\tau_{\text{ind}}/\tau| \approx 6\%$ and $|\chi_{\text{ind}}/\chi| \approx 16\%$. It should be noted that the propeller had to operate a constant n. Thus, this increase of thrust and power coefficients results in an increase of power from the electric motor.

From the previous results, it is shown that the propeller slipstream produces a significant increase on the induced lift and drag wing coefficients. However, instantaneous interaction effects also imply a strong distortion of the slipstream due to the presence of the wing, which induces local modifications in the propeller rotation plane, and thus, changes in the propeller performance.

Conclusions

This article has presented a wind-tunnel study of the interactional aerodynamics generated on a P/N/W2 ensemble operating under different flight phases as a function of β. The following major conclusions have been drawn from the results obtained in the present experimental approach on the P/N/W2 flow configurations.

For each value of β associated to a given convertible flight phase, the presence of the half-wing produces strong distortions of the tip vortex trajectories, and thus, a significant modification of the corresponding propeller wake geometry. From the present results the modifications of the axial convection velocity and radial contraction of the vortex near the wing surface have been exhibited and determined for different azimuthal position of the emitting blade tip. Such determination will aid in the design and future numerical modeling of the interaction problem.

The results obtained on the instantaneous and mean pressure distributions show that the close vortex wing surface interaction gives rise to a low-pressure peak on the wing upper side, which produces an increase in the positive local lift area near the leading edge, at each value of β = constant. Deduced from the integration of the $\overline{Cp}$ distributions, the $\overline{C_L}$ coefficient is shown to increase as β increases at all spanwise sections of the half-wing.

Concerning the reciprocal aerodynamic influence of the propeller and the half-wing the present data exhibited typical behaviors on all of the induced aerodynamic coefficients on both the wing (C_{Di}, C_{Li}, C_{Mi}) and the propeller (τ_i, χ_i). The results indicated that the propeller slipstream produces a significant increase of induced lift and drag coefficients along the half-wing span. However, when $\beta > 0$ deg, the propeller swirl influence appears to be more attenuated. On the other hand, the effect of the presence of the half-wing is to increase the τ_{ind} of the propeller. The net-induced effect on χ_{ind} appears to be more attenuated as β increases.

Acknowledgment

The authors would like to thank the Commission of European Community for Grant AERO-0029 C.

References

[1]Andres, J., Hubert, H., and Renaud, J., "The Tilt-Rotor Aircraft: A Response to the Future from European Interrogations to EUROFAR Actions," *Proceedings of 12th European Rotorcraft Forum*, Garmish-Partenkirchen, Germany, 1986 (Paper 23).

[2]Benoit, B., and Bousquet, J. M., "Aerodynamic Design of a Tilt-Rotor Blade," *Proceedings of 17th Congress of the International Council of the Aeronautical Sciences*, Stockholm, 1990, pp. 324–332 (Paper 90-521).

[3]Witkowski, P., Johnston, T., and Sullivan, P., "Propeller/Wing Interaction," AIAA Paper 89-0535, Jan. 1989.

[4]Witkowski, P., Lee, H., and Sullivan, P., "Aerodynamic Interaction Between Propellers and Wings," *Journal of Aircraft*, Vol. 26, No. 9, 1989, pp. 829–836.

[5]Johnston, R. T., and Sullivan, J. P., "The Vortex Interaction in a Propeller/Stator Flowfield," AIAA Paper 91-1818, June 1991.

[6]Crouse, G. L., Jr., Leishman, J. G., and Bi, N., "Theoretical and Experimental Study of Unsteady Rotor/Body Aerodynamic Interactions," *Journal of the American Helicopter Society*, Vol. 37, No. 1, 1992, pp. 55–65; also AIAA Paper 91-3228, Sept. 1991.

[7]Bagai, A., and Leishman, J. G., "Experimental Study of Rotor Wake/Body Interactions in Hover," *Journal of the American Helicopter Society*, Vol. 37, No. 4, 1992, pp. 48–57; also AIAA Paper 91-3232, Sept. 1991.

[8]Favier, D., and Maresca, C., "Etude du Sillage 3D d'une Hélice Aérienne," *AGARD-FDP on Aerodynamics and Acoustics of Propellers*, CP 366, AGARD, 1984, pp. 1–22 (Paper 15).

[9]Favier, D., Ettaouil, A., and Maresca, C., "Numerical and Experimental Investigation of Isolated Propeller Wakes in Axial Flight," *Journal of Aircraft*, Vol. 26, No. 9, 1989, pp. 837–846.

[10]Fratello, G., Favier, D., and Maresca, C., "Experimental and Numerical Study of the Propeller/Fixed Wing Interaction," *Journal of Aircraft*, Vol. 28, No. 6, 1991, pp. 365–373.

[11]Chiaramonte, J.-Y., Favier, D., Maresca, C., and Agnes, A., "Unsteady Interactional Effects Between a Propeller and a Fixed Wing," *Proceedings of 9th Applied Aerodynamics Conference*, AIAA, Washington, DC, 1991, pp. 237–246.

[12]Chiaramonte, J.-Y., "Etude Expérimentale et Numérique des Effets d'Interactions Instantanés sur une Configuration Hélice/Nacelle/Voilure," Ph.D. Dissertation, Univ. of Aix-Marseille II, France, Sept. 1992.